minerals

MDPI

Article

Ab initio Studies of O_2 Adsorption on (110) Nickel-Rich Pentlandite ($Fe_4Ni_5S_8$) Mineral Surface

Peace P. Mkhonto, Hasani R. Chauke * and Phuti E. Ngoepe

Received: 9 June 2015 ; Accepted: 30 July 2015 ; Published: 12 October 2015
Academic Editor: Athanasios Godelitsas

Materials Modelling Centre, University of Limpopo, Private Bag X1106, Sovenga 0727, South Africa; peace.mkhonto@gmail.com (P.P.M.); phuti.ngoepe@ul.ac.za (P.E.N.)
* Correspondence: hr.chauke@ul.ac.za; Tel.: +27-015-268-2206; Fax: +27-015-268-3268

Abstract: *Ab initio* density functional theory was used to investigate the adsorption of oxygen molecule on the nickel-rich pentlandite (110) surface, which is important for mineral extraction. The three most reactive adsorption sites: Fe-top, Ni-top, and fcc-hollow have been considered. Firstly, the non-adsorbed pentlandite surface reflects the Ni atoms relaxing inwards. Consequently, their electronic structure showed high Fe 3*d*-orbital contribution than the Ni 3*d*-orbitals at the E_F (indicating that the Fe atoms are more reactive than Ni). Secondly, the O_2-adsorbed surface predicted lowest adsorption energy for Fe-top (−1.902 eV), as a more spontaneous reaction is likely to occur than on fcc-hollow (−1.891 eV) and Ni-top (−0.040 eV) sites, suggesting Fe preferential oxidation. The density of states indicates that the O_2 show prevalence of electrons in the π_p* antibonding orbitals, and are reduced to zero states at the valence band on metal-bonded oxygen (O1). The σ_p* orbital is observed to reside just above the E_F for Fe-top and fcc-hollow site, while on Ni-top is half-occupied for both metal-bonded oxygen (O1) and terminal oxygen (O2). Finally, the isosurface charge density difference showed electron (charge) depletion on Ni/Fe metals and accumulation on the O_2 molecule. Bader analysis indicated that the oxidized Fe and Ni atoms adopt more positive charge, while O_2 on Fe-top atoms possesses more negative charge than on Ni-top, resulting with O1 possessing a smaller charge than O2 atom.

Keywords: nickel-rich pentlandite ($Fe_4Ni_5S_8$); (110) surface; oxidation; adsorption energies; density of states; Bader analysis; electronic properties; isosurface charge density

1. Introduction

Transition metal sulphides are an important group of minerals and have found application in the mining industry to meet the ever growing demand of nickel [1]. Minerals such as pyrites and pentlandite have been under investigation recently, as pentlandites are regarded a principal source of nickel [2]. Amongst others, oxygen interactions on pentlandite surface both by natural means and during flotation is an important process in mineral ore extraction. A previous investigation has reported that oxidation tends to depress the sulphide minerals [3–6] and had shown iron preferential oxidation [7]. Naturally, minerals in atmospheric contact are exposed to gaseous oxygen and this results in oxide formation. As such, oxidation of sulphide mineral surfaces is of outstanding practical importance and requires theoretical fundamental understanding of surface chemistry during mineral flotation.

The study of surface reaction on pentlandite, in particular the disordered $(Fe, Ni)_9S_8$ is not amenable using density functional theory (DFT) methods. The Fe and Ni atoms occupy a site at a certain occupancy ratio, with Fe atoms preferentially occupying the octahedral sites [8]. However, simulation of cobalt pentlandite, Co_9S_8 is relatively easier but computationally demanding since the same metal (Co) is present in all 36 metal sites in the crystal structure.

The oxidation of sulphide mineral surfaces has been investigated previously [3,4,9]. It has been indicated that the atmospheric oxidation of these minerals either by weathering or aging involves physical and chemical adsorption of oxygen on the surface and thus forms various peroxides and hydroxides. Furthermore, the oxidation products of synthetic pentlandite were found to be similar to the natural pentlandite, and are independent of the composition [3,4]. Richardson and Vaughan observed that oxidation of synthetic pentlandite under various oxidation conditions could lead to the formation of violarite ($FeNi_2S_4$) and a thin iron oxyhydroxide overlayer [9]. On the other hand, Buckley and Woods revealed that oxidation of natural pentlandite from a pyrrhotite matrix using XPS resolution, showed two doublets in the S 2*p* spectra. Furthermore, rapid oxidation of pentlandite to form thin FeOOH overlayers was also observed [4]. Again, oxidation of sulphide mineral in the presence of water has been investigated and showed the significant of oxide/hydroxide and sulphate species formation; and the formation of a sulphur-rich and nickel-rich subsurface layers [4,9,10]. As it is well known that the discharge acid mine drainage results from the oxidation of pyrite due to the formation of FeOOH species. This often causes serious environmental problems [11,12]. In order to reduce the unwanted oxidation of sulphide, it is necessary to ascertain the interaction mechanism of sulphide surfaces with O_2 in the absence of H_2O.

In this paper a computational simulation method is used to investigate the surface configurations and electronic properties of nickel-rich pentlandite mineral. The adsorption of pure oxygen molecule on the (110) $Fe_4Ni_5S_8$ surface is studied using DFT method to observe formation of reactant species and metal preferential bonding. It was found that the surface reaction between oxygen molecule and pentlandite mineral gave reasonable Fe–O and Ni–O bond distance. The oxygens (O1 and O2) show directional bonding leading to formation of superoxo species. Furthermore, Bader charge analysis of Fe and Ni metals show that the charges increase suggesting charge transfer to the oxygen molecule. This study provides the computational explanation to the mechanism of oxygen reaction with nickel-rich pentlandite mineral. Such information is important for enhancing the efficiency of mineral extraction during froth flotation, which depends mainly on the selective adhesion of air bubbles to mineral surfaces in a mineral.

2. Computational Model and Methods

2.1. Computational Model

Our simulation model is based on the geometry of the pentlandite structure with a space group of *Fm-3m* (225) [13]. An important aspect of the pentlandite structure is the presence of three metal-metal bond extending from each tetrahedral cation to form essential isolated cube cluster of tetrahedral cation, Rajamani and Prewitt [14] and Vaughan and Craig [15]. In order to simulate the surface properties precisely, different possible arrangements of the Ni and Fe atoms were considered to construct the desired $Fe_4Ni_5S_8$ pentlandite structure (Figure 1), with four octahedral metal sites occupied by Ni(O), while the 32 tetrahedral metal sites are evenly occupied by Fe(T) and Ni(T). The Ni(O) are coordinated to the face-capping sulphurs, while the Fe(T) and Ni(T) are coordinated to the linked and face-capping sulphurs. The S(l) are 4-coordinated while the S(f) are 5-coordinated.

We used the stable bulk nickel-rich pentlandite structure to cleave (110) surface. Note that different surface terminations have been considered since these display different reactivity and surface energies. Furthermore, this has an effect during adsorption, as a very reactive surface may not give a reasonable thermodynamic behaviour of the mineral surface. As such we have tested different terminations and considered the most stable surface termination (Term. 3) with lowest positive surface energy (less reactive), represented in Figure 1b. This is also based on the previous report that during the first stage of flotation where mineral particles are crushed, the minerals will mainly cleave along surfaces that have large inter-planar spacing and few inter-planar bonds, usually low-index surfaces with low surface energies under dry conditions [16]. Due to the high computational demand of the pentlandite structure, we considered a stoichiometric surface slab composed of four-layered

of atoms separated by a vacuum slab of 20 Å, which was tested and found to be sufficient to avoid interaction between slabs. The two top-most atomic layers of the substrate were allowed to relax and the bottom-most atomic layers of the substrate were fixed to the bulk coordinates in the adsorption calculations (see Figure 2). The energy required to cleave the bulk crystal exposing the surface is the surface energy and this is obtained by:

$$E_{surface} = \left(\frac{1}{2A}\right)[E_{slab} - nE_{bulk}] \quad (1)$$

where E_{slab} is the total energy of the cell containing the surface slab, E_{bulk} is the total energy of the bulk per atom, n is the number of atoms in the slab and A is the area of the cell containing the surface slab. A low positive value of $E_{surface}$ indicates stability of the surface.

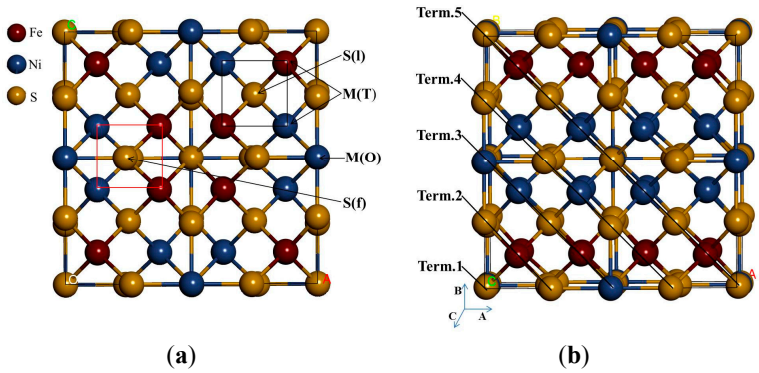

Figure 1. The crystal structure of nickel-rich pentlandite: (**a**) conventional $4(Fe_4Ni_5S_8)$ and (**b**) different terminations considered. M(O) and M(T) represent the octahedral and tetrahedral metals, respectively, with S(f) and S(l) representing the face-capping and the linked sulphurs, respectively.

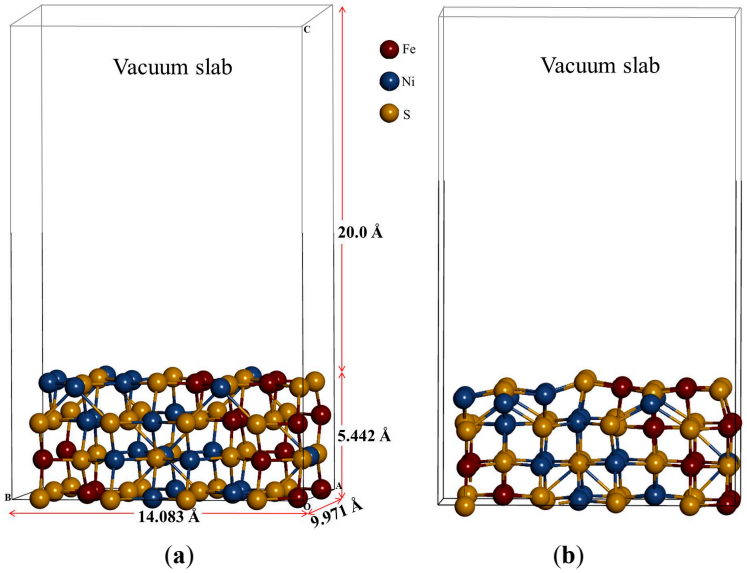

Figure 2. The side view of (110) surface: (**a**) un-relaxed and (**b**) relaxed surfaces.

2.2. Computational Methods

Ab initio quantum-mechanical density functional theory [17,18] calculations are used to investigate the surface-O_2 reaction on nickel-rich pentlandite mineral, employing VASP (Vienna Ab-initio Simulation Package) code [19]. The plane-wave (PW) pseudopotential method with

generalized gradient approximation of Perdew-Burke-Ernzerhof (GGA-PBE) exchange-correlation functional [20] was used to model surface properties of $Fe_4Ni_5S_8$ (110) surface. The ultrasoft pseudopotential is used with a plane-wave basis set truncated at a kinetic energy of 400 eV, since this was sufficient to converge the total energy of the bulk and surface systems. The equilibrium cell parameters for the bulk nickel-rich pentlandite were obtained using k-point mesh of $5 \times 5 \times 5$ to be sampled in the Brillouin zone integrations. The resulting cell parameters was 9.977 Å, which agrees well with the previously calculated value of 9.991 Å by Chauke *et al.* [21], also with the experimental value of 10.100 Å, Lindqvist *et al.* [22]. Structural optimization of the surface model were then performed using a conjugate gradients technique with an iterative relaxation of the atomic positions until the forces on the atoms were all less than 0.01 eV/Å. For all geometry optimization of the surface, a $5 \times 5 \times 1$ k-point mesh was used. This is chosen according to the scheme proposed by Monkhorst and Pack [23]. These are also employed at the final single-point runs for the calculation of the electronic spin-polarized density of states, where the spin down and spin up of the electrons are considered.

Now, in order to calculate reaction energies, the energy of the free O_2 molecule was evaluated using a $10 \times 10 \times 10$ cubic cell with similar oxygen PAW potential, cut-off energy and other equivalent precision parameters as in the surface calculations. The O_2 molecule was calculated as a spin triplet and we obtained an equilibrium bond distance d[O–O] of 1.211 Å, which correlates well with experimental bond length of 1.21 Å [24].

The charge states of the ions at the surface were discussed on the basis of a Bader analysis, which consists of integrating the electron density in a region defined for each atom in such a way that the density gradient flux through the dividing surfaces is zero [25]. An algorithm and a program developed for this purpose by Henkelman *et al.* have been employed [26,27]. The charge density difference upon adsorption was determined by calculating the charge density for the adsorbed system first and then for the (110) clean surface and finally for the O_2 molecule alone, each in the optimized geometry obtained for the adsorbed system. The difference between the charge density distribution of the adsorption system and the sum of the distribution for the (110) substrate and the O_2 adsorbate,

$$\rho\,(\text{Surface} + O_2) - \rho\,(\text{Surface}) - \rho\,(O_2) \tag{2}$$

reveals the distribution of charge upon adsorption. We have used the VESTA software [28], to visualize the charge density difference between the oxidized surface system and the clean surface plus the oxygen molecule.

3. Results and Discussions

3.1. Relaxations of the (110) Surface

Based on the stable surface geometry (Figure 3), we noted that the S(l) and S(f) atoms change from four-coordinated and five-coordinated as in the bulk to three-coordinated and four-coordinated on the surface slab, respectively. The Fe(T) and Ni(T) atoms change from four-coordinated as in the bulk to three-coordinated on the surface slab. After the surface relaxation we noted that the top layer 1 relaxes into three layers. The surface results in sulphur termination as the sulphur (S2) atoms relaxes outwards forming layer 1. The Fe atoms and S1, S3 and S4 atoms form layer 2, while Ni atoms form layer 3.

The vertical displacement of these atoms results in S1 and S3 relaxing inwards as S4 relaxes outwards. The Fe atoms are noted to have the Fe1 and Fe4 relaxing outwards minimally, as Fe2 and Fe3 remain un-displaced. Figure 3c clearly shows that the top bond length between the Ni atoms is weakened (stretches to 3.693 and 3.433 Å). The Ni atoms are observed to relax deep compared to the Fe atoms, indicating that the surface layer is composed of mainly Fe atoms. This suggests the Fe preferential oxidation character of the pentlandite [8].

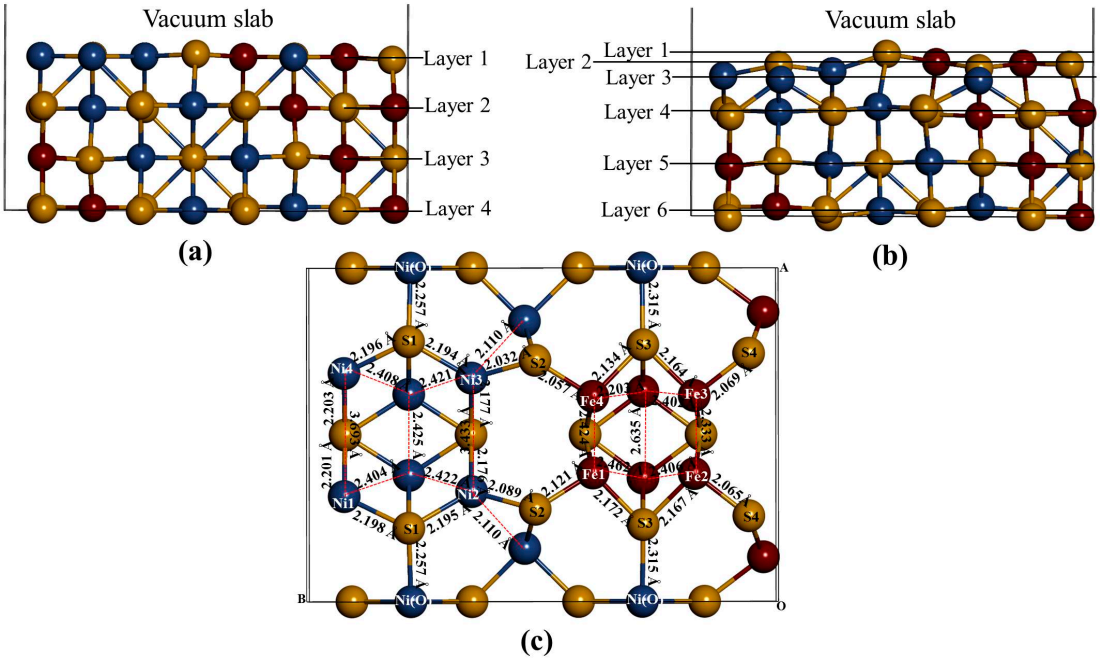

Figure 3. The (110) surface: Show side view of the layers, (**a**) before relaxation and (**b**) after relaxation and (**c**) top view after relaxation with bond distances between the top four layers.

Table 1 shows the vertical displacement of the top atoms on the surface after relaxation (negative and positive sign indicate inwards and outwards displacement, respectively). Only S2 and Fe1 have a higher outwards displacement, and Fe2 and Fe3 remains un-displaced, significantly changes the bond distances. The Ni atoms are noted to have the highest inwards displacement.

Table 1. Atomic vertical displacements (Å) of the relaxed top three layers on slab model.

Atom	Displacement
S1	−0.003
S2	+0.009
S3	−0.006
S4	+0.002
Ni1–Ni4	−0.018
N2–Ni3	−0.012
Fe1	+0.008
Fe2	0.000
Fe3	0.000
Fe4	+0.003

3.2. Electronic Structures of the Bulk and Non-Adsorbed Surface

The density of state for the bulk convectional nickel-rich pentlandite is presented in Figure 4. We noted from the total density of states (TDOS) that the spin up/down peaks are equally occupied and appear as mirror images suggesting a non-magnetic behavior, this confirms the character of the pentlandite mineral [29]. The partial density of states (PDOS) clearly shows that the *d*-orbital for Fe(T) are predominant and those of Ni(O) are lowest at the Fermi energy (E_F). We note that the octahedral Ni(O) *d*-orbital form a sharp peak at about −2.0 eV. The Fe(T) *d*-orbital peaks reside just below the E_F at the valence band (VB), while the Ni(T) *d*-orbital contribution is very low at the E_F. At the conduction band (CB), the Ni atoms have very little contribution while the Fe atoms show a peak at around 2.0 eV.

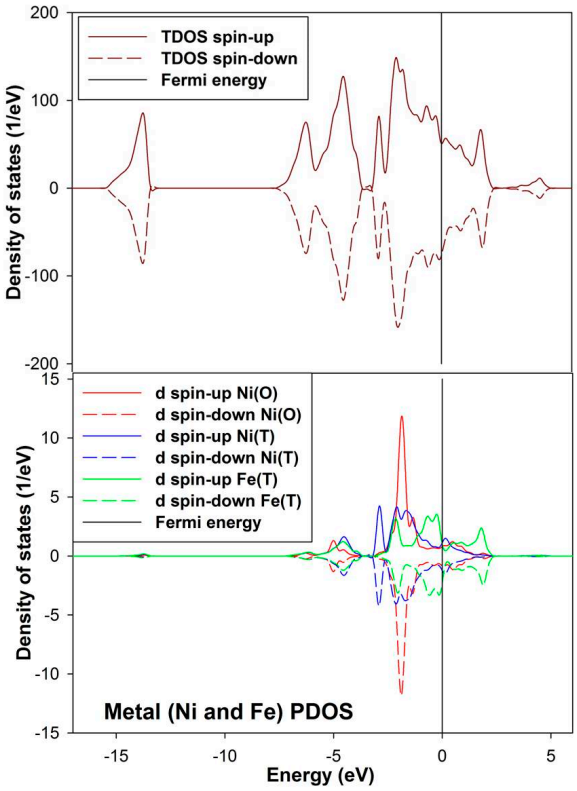

Figure 4. Projection total and partial density of states for the tetrahedral metals (Ni(T) and Fe(T)) and octahedral metals (Ni(O)) in the bulk conventional 4($Fe_4Ni_5S_8$) nickel-rich pentlandite.

Figure 5a show density of states (DOS) of (110) surface and it is evident from the total density of states (TDOS) that the *d*-orbital of the metals (M) are the centre of reactivity on the surface as they highly dominate more at the E_F. Moreover, the TDOS shows that the surface has a metallic behavior characteristic as there is no band gap at the E_F and still shows a non-magnetic character. Note that the partial density of states (PDOS) is plotted only for the top metals (*i.e.*, Fe and Ni) atoms adsorbed. The PDOS demonstrates that both the Ni and Fe atoms provide accessible bands at the E_F. This indicates that the electrons are delocalized, and that the Ni atoms contribute considerably to this delocalization.

Now considering the PDOS (Figure 5a), we note different feature with respect to both top Ni and Fe atoms. Note that we show the PDOS of the Ni and Fe atoms where adsorption will take place. Firstly, the behavior of Ni2–Ni3 *d*-orbital is observed to move closer to the E_F and its contribution is characterized by a sharp *d*-orbital peak near E_F at the (VB) (compared to the Ni(O) in the bulk) with very little contribution at the E_F and at the (CB). Secondly, the Fe1–Fe4 PDOS are noted to have five *d*-orbital peaks, three at the VB and two at the CB. We observed that the *d*-orbital moves across the E_F, where the E_F cuts the highest states peak, and we also noted two broad peaks, *i.e.*, the highest states peak (at about 0.05 eV) and the second highest states peak (at about 2.0 eV). It is clear that the bulk *d*-orbital contribution for both tetrahedral and octahedral metals is different than the surface metals. The bulk tetrahedral coordinated metals show predominance of states in the VB, while states are shifted towards the E_F for the surface metals.

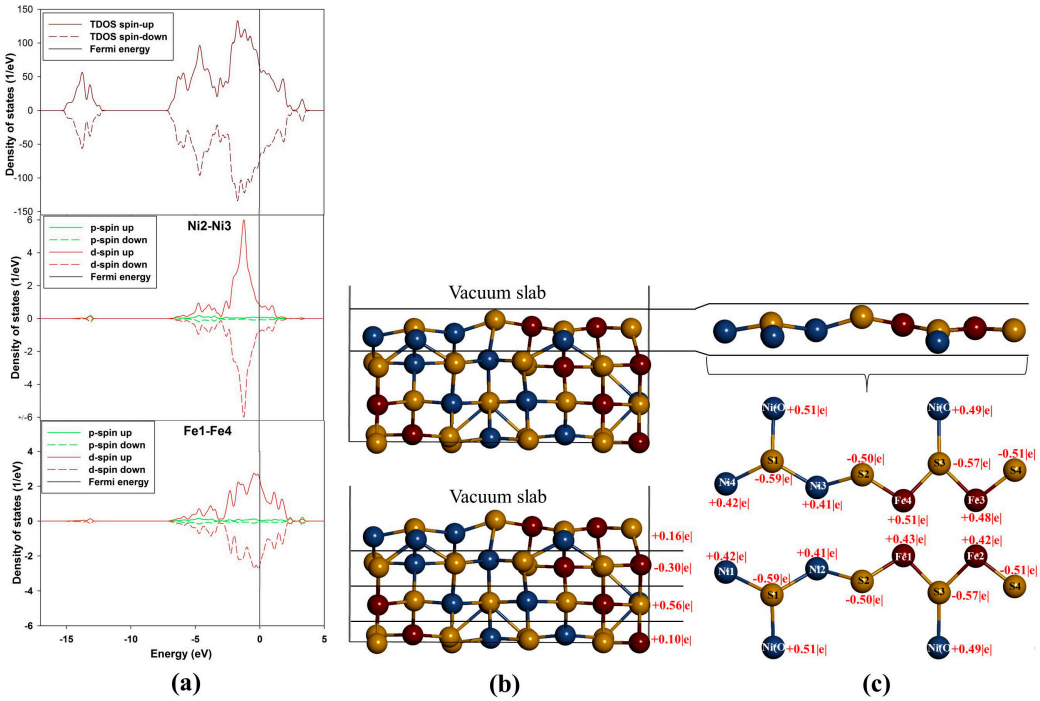

Figure 5. Projection density of states and Bader charges for the top adsorbed Ni and Fe atoms: (**a**) total and partial density of states; (**b**) Bader charges for each layer and (**c**) Bader charges for the top layer atoms.

The Fe atoms on (110) surface are observed to have different Bader charges (Figure 5c). This difference indicates that the Fe atoms are not charge ordered and there is alternation of the charges on the Fe atoms. Furthermore, this suggests that the presence of Ni atoms breaks the charge symmetry of the Fe atoms to a small degree, such that the Fe atoms with $Fe^{+0.42|e|}$ have $0.09|e|$ less than the $Fe^{+0.51|e|}$. Such observations of the charge symmetry breakage have been observed on doping of FeS with Ni by Devey *et al.* [30]. Now, for the case of Ni atoms, we observed that Ni1–Ni4 have the same charges and so are Ni2–Ni3 atoms. Thus, by analogy it can be deduced that there is a high level of covalent nature predicted for the Ni–S and Fe–S bonds in $Fe_4Ni_5S_8$ pentlandite. The Bader charges of the metals shown in Figure 5c indicate that the Fe atoms carry more positive charges than the Ni atoms. The three outermost layers are positively charged, while the second layer is electronegative (Figure 5b).

3.3. Free O_2 Molecule

The ground state of free O_2 molecule is experimentally found to be a spin triplet state, and the equilibrium bond length is 1.21 Å [24], this compares well with our predicted value 1.211 Å. In order to get more information about the electronic structure of the oxygen molecule, we analyze the density of states (DOS) of free O_2 molecule in Figure 6. The energy level of the occupied orbitals of free oxygen molecule shows a band gap between the highest occupied molecular orbitals (HOMO) and the lowest unoccupied molecular orbitals (LUMO), referred to as HOMO-LUMO (H-L) gap. Our predicted H-L gap is 1.3 eV, this is low compared to the H-L gap of 2.27 eV using PBE [31]. However, it has been reported that HSEO6 and PBEO hybrid functionals widen the H-L gap [31]. The current H-L gap suggests that the small value is significant and may suggest that the O_2 will react strongly with the surface. This correlates with previous literature that the chemical reactivity of a molecule is dependent on the H-L gap [32].

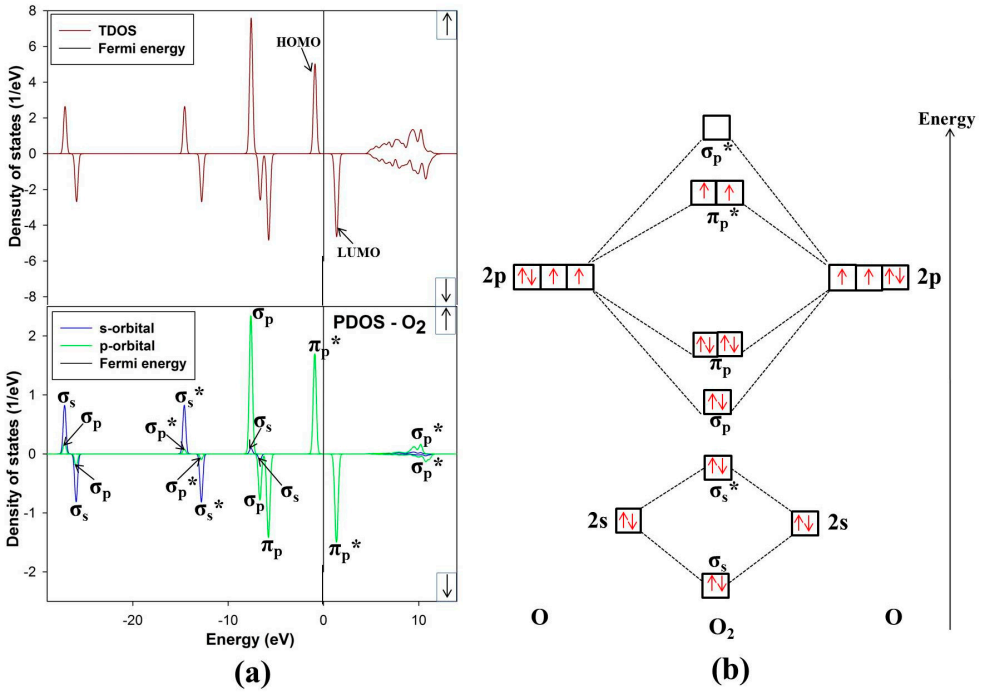

Figure 6. (**a**) Total and partial density of states and (**b**) molecular electron configuration of free O_2 molecule.

The energy levels of the molecular orbitals for O_2 especially that of the *p*-orbital LUMO peak, play an important role in the initial adsorption for O_2 on the nickel-rich pentlandite surface. This is so because O_2 accepts electrons from the mineral surface through the LUMO π_p* antibonding [26]. Figure 6 of free-O_2 clearly illustrates the versatility of O_2. We note that not only σ and π orbitals; bonding and antibonding orbitals are present but also a significant spin splitting of the levels. This clearly shows the significance of Hund's first rule, since the antibonding spin-up π_p* orbitals are occupied and the spin-down ones are empty reflecting that O_2 molecule in its ground state is a spin triplet. We also noted some *s-p* hybridization, particularly for the 2*s* derived σ_s and σ_s* orbitals, these observations have been previously reported [33].

3.4. O_2 Adsorption

Now we evaluate the effect of O_2 molecule adsorbed on the (110) surface, considering three distinct adsorption trajectories as shown in Figure 7. The three sites fcc-hollow, Ni-top, and Fe-top are the possible active adsorption sites. The oxygen molecule is positioned vertical on the surface and the O–O bond length is optimized at each height. In this case the reaction co-ordinate is the height from surface to oxygen molecule. The adsorption strength on interaction of O_2 and the substrate is calculated as,

$$E_{adsorption} = E_{system} - (E_{slab} + E_{adsorbate}) \quad (3)$$

where E_{system} is the energy of the surface slab with adsorbate, E_{slab} is the energy of the slab and $E_{adsorbate}$ is the energy of the free O_2 molecule. Note that a negative value shows a spontaneous exothermic reaction between the oxygen molecule and the surface, whereas a positive value reveals the opposite.

In considering the adsorption of O_2 at fcc-hollow site (Figure 8a); we noted that the oxygen molecule forms a bridging bond with Fe atoms (Fe1–O_2–Fe4). This observation suggests the preferential oxidation of Fe atoms, and similar results have been previously reported by Merape *et al.* [8]. A bond angle of 84.68° was noted on the bridge bond and compares well with the previous studies of Wang *et al.* [34], where a bond angle of 81.9° was reported. The difference of 2.78

between these two bond angles may be due to the fact that unlike in the current study an oxygen atom was adsorbed instead of the oxygen molecule. This also had an effect on the Fe1–Fe4 bond length, which increased from 2.292 to 2.449 Å. The bond lengths of Fe1–O1 and Fe4–O1 are similar (1.818 Å), which is smaller than the radius between Fe–O of 1.920 Å. This indicated a strong electron overlap across Fe1–O1 and Fe4–O1.

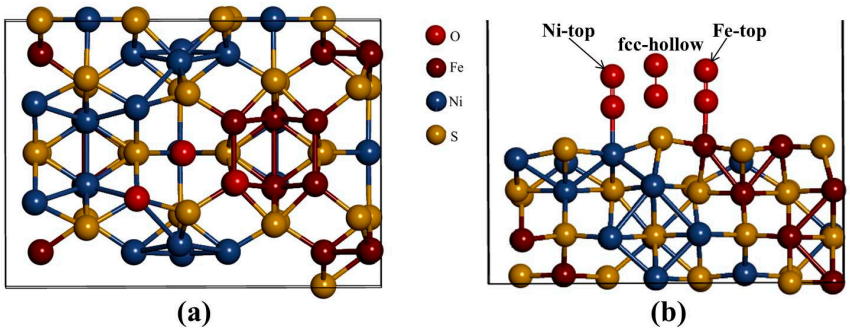

Figure 7. (**a**) Top view and (**b**) side view of the three different adsorption geometries investigated: fcc-hollow, Fe-top, and Ni-top.

The adsorption of O_2 on Fe-top site (Figure 8a) showed similar behavior as observed for fcc-hollow site. However, the resulting bond lengths of Fe1–O1 and Fe4–O1 are different with 1.815 Å and 1.817 Å, respectively (Table 2). Again these values are smaller than the radius between Fe–O of 1.920 Å, suggesting a strong electron overlap across Fe1–O1 and Fe4–O1. The bond angle of Fe1–O1–Fe4 was found to be 84.96° slightly higher than that of fcc-hollow. The oxygen bond length (O1–O2) for both fcc-hollow site and Fe-top site is found to increase to 1.316 Å, which indicates weakening of the O_2 bond. This corresponds to the report that the back donation of an electron from Fe *d*-orbital to oxygen π_p* antibonding molecular orbitals generates the diminishing of the O–O bond and lowers the bond strength of oxygen molecule [35].

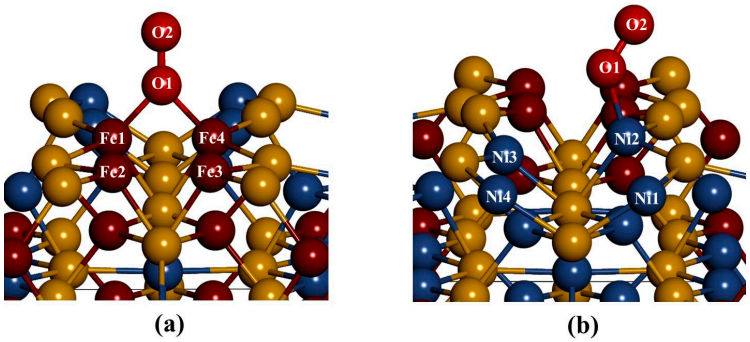

Figure 8. The relaxed geometries of O_2 molecule on the surface: (**a**) fcc-hallow site and Fe-top site and (**b**) Ni-top site.

Table 2. Variation of bond distances between O and metal (M) atoms of the mineral (110) surfaces after adsorption.

Bond Distances	Fcc-Hollow	Fe-Top	Ni-Top
Bonds	Fe–O	Fe–O	Ni–O
$d_o = r_o + r_{metal}$ (Å)	1.920	1.920	1.840
d_{ads} (Å)	1.818	1.815 and 1.817	1.801
$\Delta d = d_{ads} - d_o$(Å)	−0.102	−0.105 and −0.103	−0.039

d_o is the theoretical value, r_o is the radius of O for O_2; r_{metal} is atomic radius of metal for sulphide, d_{ads} is the distance between O atom for O_2 and metal atom of mineral surface after adsorption.

The adsorption on Ni-top (Figure 8b) shows that the oxygen molecule bends and forms an orientation of a superoxo. Furthermore, we observed that O_2 moves the Ni atom to the outermost layer, forming a Ni2–O1 bond distance of 1.801 Å, which is smaller than the radius between Ni–O of 1.840 Å. This suggested a strong electron overlap across Ni2–O1. We also found an O1–O2 bond distance of 1.284 Å and a Ni2–O1–O2 bond angle of 128.78°. This observation is in line with the previous studies by Gutsev *at al*. [36]. A Ni superoxo isomer, Ni-O bond lengths of 1.728 Å and O–O of 1.284 Å and a Ni–O–O bond angle of 125.3° were reported. Similarly, Citra *et al.* [37], found Ni–O (1.721 Å), O–O (1.302 Å) and Ni–O–O (123.0°). Also Uzunova *et al.* [38], found Ni–O and O–O of 1.722 Å and 1.272 Å, respectively and a Ni–O–O bond angle of 126.3°. These findings compared well with the current results and confirm a neutral superoxo isomer species forming on the surface.

Table 2 present the change in distances (Δd) between O atom (of O_2 molecule) and adsorbed-metal atom of the mineral surface (d_{ads}) compared with the sum of the atomic radius of O atom and adsorbed-metal atom (d_o). We noted that the distance between O and Fe atoms decrease (−0.102 Å), indicating strong interaction between O_2 molecule and top layer Fe atoms. The distance between O atom and Ni atom also slightly changes (−0.039 Å). These results indicate that Fe oxidize rapidly than Ni atoms.

Table 3 list the surface and adsorption energies of the nickel-rich pentlandite (110) surface. Adsorption of O_2 is found to be an exothermic process (the reaction happens spontaneously). The adsorption strength of O_2 on the surface is found to be stronger on the Fe-top (−1.902 eV) than fcc-hollow site (−1.891 eV) and Ni-top (−0.040 eV). Clearly the Fe-top is more exothermic than fcc-hollow by 0.011 eV, suggesting that some energy is lost in the chemisorption process on fcc-hollow site. It is thus evident that the adsorption energy of Fe atoms is more spontaneous than on Ni atoms, confirming the preferential oxidation of Fe.

Table 3. Calculated surface and adsorption energies.

Surface	Surface Energy	Adsorption (Ads.) Energies		
	$E_{(surface)}$ (eV/Å^2)	$E_{(Ads.)}$ (eV)		
(110)	0.061	fcc-hollow	Ni-top	Fe-top
		−1.891	−0.040	−1.902

3.5. Electronic Structure of O_2 Adsorbed Surface

The density of states has been calculated to describe the interaction between the O_2 molecule and the nickel-rich pentlandite mineral (110) surface (Figure 9a,b). Note that we only discuss the DOS for adsorption on Fe-top and Ni-top, since the fcc-hollow showed similar behavior as the Fe-top site. The TDOS is characterized by three spin up/down broad peaks at the VB at −2.0, −5.0 and −14.0 eV, where the −2.0 eV peaks clearly emanate from 3*d* hybridization with O_2 π_p* orbital. A clear distinction is noticed on the PDOS depicting effects of O_2 adsorption on metal atoms. The LUMO π_p* moves to the VB, clearly illustrated that the adsorption of O_2 on the surface is initiated by accepting electrons from the mineral surface into the LUMO π_p* antibonding orbital. This charge transfer is in the form of back-donation of electrons from the mineral surface *d*-orbital to the π_p* anti-bonding orbital, confirming report by Blyholder *et al.* [39].

In Figure 9a, the PDOS for Fe display three dominant spin up/down peaks near E_F at the VB, while only one peak for Ni2 *d*-orbital contribution is observed in Figure 9b. This may suggest strong hybridization of Fe 3*d* with O 2*p* orbital and less for Ni 3*d*. It is also clear that the M-bonded oxygen (O1) and terminal oxygen (O2) PDOS are different for Fe and Ni interaction. The Fe–O_2 interaction shows a single peak of σ_p-orbital (equal states for both O1 and O2) and double degenerate π_p-orbital. The Ni–O_2 interaction shows a single peak of σ_p-orbital and a single degenerate π_p-orbital. More importantly for Fe–O_2, the O1 π_p-orbital peak is two degenerate and becomes reduced for the case of O2 π_p-orbital peak. The single σ_p-orbital peak becomes dominant for O2 PDOS. This behavior is

different for Ni and O interaction (Figure 9b), displaying singlet degenerate π_p and σ_p peaks in the VB. However, σ_p and π_p orbital shows strong overlap for O1.

The other contribution peaks are noticed at energies −25.0 and −16.0 eV for Fe-top and −25.0 and −15.0 for Ni-top, which are of σ_s and σ_s* character, respectively. Furthermore, O2 contribution for both case are also distinct, a sharp π_p* peak and broad π_p* (reduced states) peak are observed at about −2.0 eV for Fe and Ni, respectively. The PDOS on O1 is observed to have the π_p* peaks reduced to zero states at −2.0 eV, while the σ_p* peaks reside just above the E_F and is half-occupied at the E_F for Fe–O_2 and Ni–O_2, respectively. The half occupancy of the σ_p* orbital have been observed previously on O_2 adsorption on Al(111) surface [40].

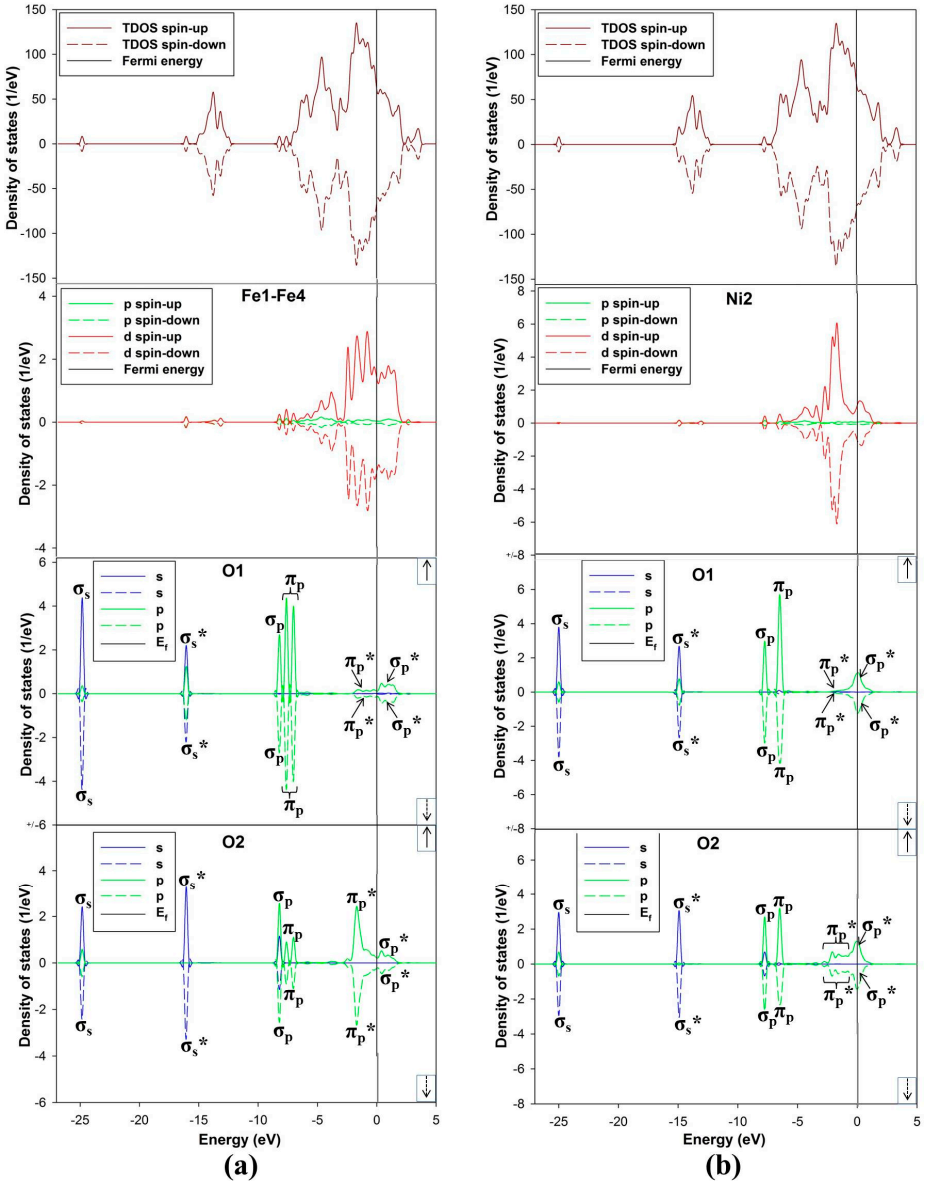

Figure 9. The density of states (DOS) TDOS and PDOS: (**a**) adsorption on Fe-top site and (**b**) adsorption on Ni-top site.

Figure 10a,b display the charge density difference, for the Fe-top and Ni-top adsorption sites. We observed that the Fe and Ni atoms donate electrons while O_2 accept. This is due to a formation of negative electronic cloud (charge depletion) while the O_2 has a positive electronic cloud (charge accumulation). The cylindrical shape around O2 atom represents the π_p* orbital, as observed from the

PDOS and it signifies a superoxo bonding mode. Similar observation has been formed in the studies by Yoon *et al.* [41].

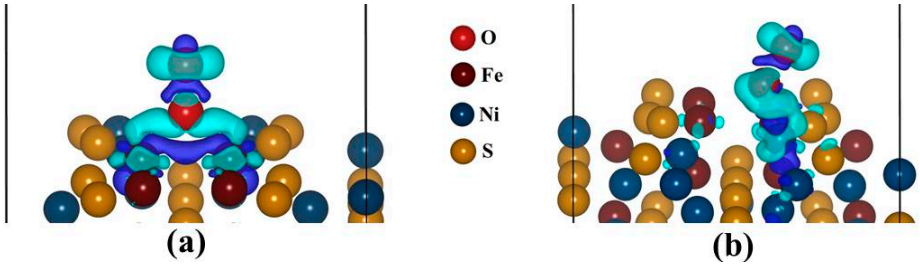

Figure 10. The sketch of isosurface charge density difference: (**a**) Fe-top site (isosurface level = 0.004 eÅ^{-3}) and (**b**) Ni-top site (isosurface level = 0.003 eÅ^{-3}). Cyan represents positive electronic clouds which accept electrons and blue stands for negative electronic clouds which donate electrons.

Now, we use Bader analysis to examine the electron transfer from the surface Fe and Ni atoms to the oxygen molecule, in the fcc-hollow, Fe-top and Ni-top sites. Interestingly, we found that in all cases the oxidized Fe and Ni atoms adopts more positive charge. For fcc-hollow: Fe1 = Fe4 = +0.72 |e|, Fe-top: Fe1 = +0.72 |e| and Fe4 = +0.71 |e| and for Ni-top: Ni2 = +0.64 |e|, which indicates that an electron has been donated to the O_2 molecule. This is due to a negative electronic cloud (charge depletion) on the Fe and Ni atoms while the O_2 has a positive electronic cloud (charge accumulation), as observed from the charge density difference in Figure 10a,b. The cylindrical shape around O2 atom, represent the π_p* orbital and this signifies a superoxo bonding mode, similarly to the PDOS observation (Figure 9a,b). The oxygen molecule possesses negative charges: for fcc-hollow (O1 = −0.48 |e| and O2 = −0.18 |e|), Fe-top (O1 = −0.48 |e| and O2 = −0.15 |e|) and for Ni-top (O1 = −0.25 |e| and O2 = −0.12 |e|). It is clear that the terminal oxygen (O2) has a smaller charge than the M-bonded oxygen atom (O1). This charge distribution behavior for superoxide has been previously reported [38]. The charge on O_2 (*i.e.*, charge sum of O1 and O2), for lowest ground state are as: for fcc-hollow (−0.66 |e|), for Fe-top (−0.63 |e|) and for Ni-top (−0.37 |e|). It clearly shows that O_2 on Fe atoms possesses more negative charge than on Ni atom. The negative charge on the oxygen atoms is also confirmed by experiment for superoxo or end-bonded O_2 [42].

4. Summary and Conclusions

The O_2 adsorption on nickel-rich pentlandite (110) surface has been investigated using DFT for three adsorption sites: fcc-hollow, Fe-top and Ni-top. Firstly, the optimized non-adsorbed surface was observed to have Ni atoms relaxing inward into the surface. As a result their DOS showed less contribution of Ni 3*d*-orbital contribution at E_F, while the Fe atoms contribute more, indicating that the Fe atoms are more reactive than the Ni. Secondly, the O_2 adsorption for all cases is spontaneous reaction (exothermic), with Fe-top being more favorable with adsorption energy of −1.902 eV, compared to fcc-hollow (−1.891 eV) and Ni-top (−0.040 eV). This suggested a preferential oxidation of Fe than Ni.

The DOS, Bader analysis and isosurface charge density difference were computed for the O_2 adsorbed surface. The DOS for fcc-hollow and Fe-top showed similar trend, displayed two degenerate π_p orbital peaks, while for Ni-top a single degenerate π_p peak was observed at the VB. In all three adsorption sites cases, their π_p* peak at −2.0 eV reduced to zero state for O1 atom, while the σ_p* peaks reside just above the E_F for fcc-hollow and Fe-top and is half-occupied for Ni-top on both O1 and O2. The O_2 interaction with Fe1 and Fe4 atoms on the top surface, showed three sharp 3*d*-orbital peaks at the VB and a broad peak at the CB (between −2.5 and 1.5 eV), while Ni2 is observed to have a sharp peak at the VB (at around −2.0 eV) and a small peak at the E_F. The isosurface charge density

difference and Bader analysis showed the difference in electron (charge) depletion and accumulation between the top surface (Fe and Ni) and the O_2. In particular, the charge density difference showed directional bonding, a cylindrical shape cloud on O2 was observed, suggesting a superoxo bonding. Finally, Bader analysis, in all cases indicated that the oxidized Fe and Ni atoms adopts more positive charge, while O_2 on Fe atoms possesses more negative charge than on Ni atom. Interestingly, the M-bonded oxygen (O1) has smaller charge than the terminal oxygen (O2).

Acknowledgments: The research was funded by the South African Minerals to Metals Research Institute (SAMMRI) and Department of Science and Technology (DST). The research work was performed at the Materials Modelling Centre (MMC), University of Limpopo; and also benefited from supercomputing resources at the Centre for High Performance Computing (CHPC) in Cape Town. The support of the South African Research Chair Initiative of the Department of Science and Technology and the National Research Foundation is highly recognized. Further gratitude is expressed to the industrial advisors, Jules Aupiais and Neville Plint.

Author Contributions: P.E.N. and H.R.C. conceived and designed the computational approaches used in the paper; P.P.M. performed the calculations towards his thesis project. All authors, P.P.M., H.R.C. and P.E.N. contributed to the writing and analysis of the paper.

Conflicts of Interest: The authors declare no conflict of interest.

References

1. Ngobeni, W.A.; Hangone, G. The effect of using sodium di-methyl-dithiocarbamate as a co-collector with xanthates in the froth flotation of pentlandite containing ore from Nkomati mine in South Africa. *Miner. Eng.* **2013**, *54*, 94–99. [CrossRef]
2. Cabri, L.J. Platinum-group elements: Mineralogy, geology and recovery. *Can. Inst. Min. Metall. CIM Spec.* **1989**, *23*, 199–217.
3. Legrand, D.L.; Bancroft, G.M.; Nesbitt, H.W. Oxidation/alteration of pentlandite and pyrrhotite surface at pH 9.3: Part 1. Assignment of XPS spectra and chemical trends. *Am. Miner.* **2005**, *90*, 1042–1054. [CrossRef]
4. Buckley, A.N.; Woods, R. Surface composition of pentlandite under flotation related condition. *Surf. Interface Anal.* **1991**, *17*, 675–680. [CrossRef]
5. Heiskanen, K.; Kirjavainen, V.; Laapas, H. Possibilities of collectorless flotation in the treatment of pentlandite ores. *Int. J. Miner. Process.* **1991**, *33*, 263–274. [CrossRef]
6. Kelebek, S.; Nanthakamar, B. Characterrization of stockpile oxidation of pentlandite and pyrrhotite through kinetic analysis of their flotation. *Int. J. Miner. Process.* **2007**, *84*, 69–80. [CrossRef]
7. Merape, G. Fundamental Electrochemical Behaviour of Pentlandite. Master's Thesis, University of Pretoria, Pretoria, South Africa, August 2010.
8. Knop, O.; Huang, C.H.; Woodhams, F.W.D. Chalcogenides of transition elements. VII. A mossbauer study of pentlandite. *Am. Miner.* **1970**, *55*, 1115–1130.
9. Richardson, S.; Vaughan, D.J. Surface alteration of pentlandite and spectroscopic evidence for secondary violarite formation. *Mineral. Mag.* **1989**, *53*, 213–222. [CrossRef]
10. Sit, H.L.P.; Cohen, M.H.; Selloni, A. Interaction of oxygen and water with the (100) surface of pyrite: Mechanism of sulphur oxidation. *J. Phys. Chem. Lett.* **2012**, *3*, 2409–2414. [CrossRef] [PubMed]
11. Rimstidt, J.D.; Vaughan, D.J. Pyrite oxidation: A state-of-the-art assesment of the reaction machanism. *Geochim. Cosmochim. Acta* **2003**, *67*, 873–880. [CrossRef]
12. Evangelou, V.P. *Pyrite Oxidation and Its Control*, 1st ed.; CRC Press: New York, NY, USA, 1995; pp. 1–295.
13. Geller, S. Refinement of the crystal structure of Co_9S_8. *Acta Crystallogr.* **1962**, *15*, 1195–1198. [CrossRef]
14. Rajamani, V.; Prewitt, C.T. Crystal chemistry of natural pentlandites. *Can. Miner.* **1973**, *12*, 178–187.
15. Vaughan, D.J.; Craig, J.R. *Mineral Chemistry of Metal Sulphides*; Cambridge University Press: Cambridge, UK, 1978.
16. Mkhonto, D.; Ngoepe, P.E.; Cooper, T.G.; de Leeuw, N.H. A computer modelling study of the interaction of organic adsorbates with fluorapatite surfaces. *Phys. Chem. Miner.* **2006**, *33*, 314–331.
17. Hohenberg, P.; Kohn, W. Inhomogeneous electron gas. *Phys. Rev. B* **1965**, *136*, 864–871. [CrossRef]
18. Hohenberg, P.; Kohn, W. Density functional theory. *Phys. Rev. B* **1964**, *136*, 864–876. [CrossRef]
19. Kresse, G.; Furthermüller, J. Efficient iterative schemes for ab-initio total-energy calculations using a plane-wave basis set. *Phys. Rev. B* **1996**, *54*, 11169–11186. [CrossRef]

20. Perdew, J.; Burke, K.; Ernzerhof, M. Generalized gradient approximation made simple. *Phys. Rev. Lett.* **1996**, *118*, 3865–3868. [CrossRef]
21. Chauke, H.R.; Nguyen-Manh, D.; Ngoepe, P.E.; Pettifor, D.G.; Fries, S.G. Electronic structure and stability of the pentlandites Co_9S_8 and $(Fe,Ni)_9S_8$. *Phys. Rev. B* **2002**, *66*, 1–5. [CrossRef]
22. Lindqvist, M.; Lundqvist, D.; Westgren, A. Crystal structure of Co_9S_8 and of pentlandite $(Ni,Fe)_9S_8$. *Svensk Kemisk Tidskrift* **1936**, *48*, 60–156.
23. Monkhorst, H.F.; Park, J.D. Special points for Brillouin-Zone integrations. *Phys. Rev. B* **1976**, *13*, 5188–5192. [CrossRef]
24. Weast, R. *CRC Handbook of Chemistry and Physics*, 86th ed.; CRC Press Inc.: Boca Raton, FL, USA, 1985; pp. 1098–4178.
25. Bader, R.F.W. *Atoms in Molecules: A Quantum Theory*; Oxford University Press: London, UK, 1994.
26. Sanville, E.; Kenny, S.D.; Smith, R.; Henkelman, G. An improved grid-based algorithm for Bader charge allocation. *J. Comput. Chem.* **2007**, *28*, 899–908. [PubMed]
27. Henkelman, G.; Arnaldsson, A.; Jonsson, H. A fast and robust algorithm for Bader decomposition of charge density. *Comput. Mater. Sci.* **2006**, *36*, 354–360. [CrossRef]
28. Momma, K.; Izumi, F. VESTA: A Three-Dimensional Visualization System for Electronic and Structural Analysis. *J. Appl. Crystallogr.* **2008**, *41*, 653–658. [CrossRef]
29. Pentlandite Wikipedia. Available online: http://en.wikipedia.org/wiki/Pentlandite (accessed on 25 May 2015).
30. Devey, A.J.; de Leeuw, N.H. Computer Modelling Studies of Mackinawite, Greigite and Cubic FeS. Ph.D. Thesis, University College London, London, UK, October 2009.
31. Liu, H.; Xiang, H.; Gong, X.G. First principles study of adsorption of O_2 on Al surface with hybrid functionals. *J. Chem. Phys.* **2011**, *135*, 1–5. [CrossRef] [PubMed]
32. Periyasamy, G.E.; Durgun, R.J.Y.; Remacle, F. DFT studies of solvation effects on the nanosize bare, thiolated and redox active ligated Au55 cluster. *J. Phys. Chem.* **2010**, *38*, 15941–15950.
33. Yourdshahyan, Y.; Razaznejad, B.; Lundqvist, B.I. Adiabatic potential-energy surface for oxygen on Al(111). *Phys. Rev. B* **2001**, *65*, 1–17. [CrossRef]
34. Wang, L. Photodetachment photoelectron spectroscopy of transition oxide species. *Adv. Ser. Phys. Chem.* **2000**, *10*, 854–957.
35. Rosso, K.M.; Becker, U.; Hochella, M.F. The interaction of pyrite (100) surfaces with O_2 and H_2O: Fundamental oxidation mechanisms. *Am. Miner.* **1999**, *84*, 1549–1561.
36. Gutsev, G.L.; Rao, B.K.; Jena, P. Systematic study of oxo, peroxo, and superoxo isomers of 3d-metal dioxides and their anions. *J. Phys. Chem. A* **2000**, *104*, 11961–11971. [CrossRef]
37. Citra, A.; Chertihin, G.V.; Andrews, L. Reactions of laser-ablated nickel atoms with dioxygen. Infrared spectra and density functional calculations of nickel oxides NiO, ONiO, Ni_2O_2, and Ni_2O_3, superoxide NiOO, peroxide $Ni(O_2)$, and higher complexes in solid argon. *J. Phys. Chem. A* **1997**, *101*, 3109–3118. [CrossRef]
38. Uzunova, E.L.; Mikosch, H.; Nikolov, G.S. Electronic structure of oxide, peroxide, and superoxide clusters of the 3d elements: A comparative functional study. *J. Chem. Phys.* **2008**, *128*, 094307. [CrossRef] [PubMed]
39. Blyholder, G.; Head, J.; Ruette, F. Semi empirical Calculation of Iron-Oxygen Interactions. *Inorg. Chem.* **1982**, *21*, 1539–1545. [CrossRef]
40. Yourdshahyan, Y.; Razaznejad, B.; Lundqvist, B.I. Adiabatic potential-energy surface of O_2/Al(111): Rare entrance-channel barriers but molecularly chemisorbed state apt for abstraction. *Solid State Commun.* **2001**, *117*, 531–535. [CrossRef]
41. Yoon, B.; Hakkinen, H.; Landman, U. Interation of O_2 with Gold Cluster: Molecular and Dissociative Adsorption. *J. Phys. Chem. A* **2003**, *107*, 4066–4071. [CrossRef]
42. Lever, A.B.P.; Ozin, G.A.; Gray, H.B. Electron transfer in metal–dioxygen adducts. *Inorg. Chem.* **1980**, *19*, 1823–1824. [CrossRef]